Predicting Energy Loss and Permeability of Field-Annealed Amorphous and Nanocrystalline Alloys up to 1 GHz

IEEE Access
Multidisciplinary ⋮ Rapid Review ⋮ Open Access Journal

Received 9 August 2024, accepted 8 September 2024, date of publication 17 September 2024, date of current version 30 September 2024.

Digital Object Identifier 10.1109/ACCESS.2024.3462747

RESEARCH ARTICLE

Predicting Energy Loss and Permeability of Field-Annealed Amorphous and Nanocrystalline Alloys up to 1 GHz

CARLO STEFANO RAGUSA[1], (Senior Member, IEEE), SAMUEL DOBÁK[2], (Member, IEEE), CINZIA BEATRICE[3], LUIGI SOLIMENE[1], (Member, IEEE), ALESSANDRO MAGNI[3], AND FAUSTO FIORILLO[3]

[1]Department of Energy, Politecnico di Torino, 10129 Turin, Italy
[2]Faculty of Science, Institute of Physics, P. J. Šafárik University, 04154 Košice, Slovakia
[3]Advanced Materials Metrology and Life Science Division, Istituto Nazionale di Ricerca Metrologica, 10135 Turin, Italy

Corresponding author: Carlo Stefano Ragusa (carlo.ragusa@polito.it)

This work was supported in part by the Project 19ENG06 Metrology of Magnetic Losses in Electrical Steel Sheets for High-Efficiency Energy Conversion (HEFMAG), funded by the European Metrology Programme for Innovation and Research (EMPIR) Program, co-financed by the Participating States and from the European Union's Horizon 2020 Research and Innovation Program; and in part by the Project Quality of Education and Development of Skills of Ph.D. Students and Postdocs at P. J. Šafárik University (KVARK), through the European Social Fund and the National Scholarship Program of the Slovak Republic, under Grant ITMS 26110230084.

ABSTRACT Crucial limitations on the permissible energy dissipation are one main factor hindering the use of soft magnetic cores at high frequencies. However, applications find limited support in present-day empirical magnetic loss models, which can hardly afford seamless high-frequency extrapolation of the predicting tools available at low frequencies. This is the case, for example, of very thin soft magnetic plates and ribbons, where the rise of eddy currents and their shielding effects at high frequencies must be attuned to the rate-dependent magnetic constitutive equation of the material. We provide in this work a comprehensive broadband (DC-1 GHz) magnetic characterization and the associated physical modeling of the energy loss and permeability properties of different types of amorphous and nanocrystalline ribbons, 6 μm to 25 μm thick, endowed with transverse induced anisotropy (7 – 251 J/m^3) and well-defined transverse domain structure. The achieved condition of quasi-linear response and excellent broadband soft magnetic properties is shown to conform to an analytical treatment of the dynamics of the magnetization process, which is mostly accomplished by moment rotations and increasingly so under increasing frequencies. By virtue of their spatially homogeneous character, rotations provide a loss contribution matching the classical loss framework. Its broadband calculation by Maxwell's diffusion equation is carried out by introducing a rate-dependent magnetic constitutive equation of the material, worked out in terms of complex susceptibility using the Landau-Lifshitz equation. The separation between domain wall (low frequencies) and rotational (high frequencies, including spin damping and eddy currents) loss contributions is eventually obtained across a many-decade-wide frequency range.

INDEX TERMS Magnetic losses, loss decomposition, amorphous alloys, nanocrystalline alloys.

I. INTRODUCTION

The versatile operating modes imposed on magnetic cores employed in power electronics and the present-day evolution towards increasing operating frequencies, up to the MHz range [1], stimulated by the need for miniaturization and the appearance of the fast silicon carbide (SiC) and gallium nitride (GaN) switching components, pose challenges in materials choice [2], characterization method [3], [4], and theoretical modeling [5], [6], [7], [8], [9]. Soft ferrites are the standard choice for high-frequency cores, thanks to their combination of low magnetocrystalline anisotropy and very

The associate editor coordinating the review of this manuscript and approving it for publication was Montserrat Rivas.

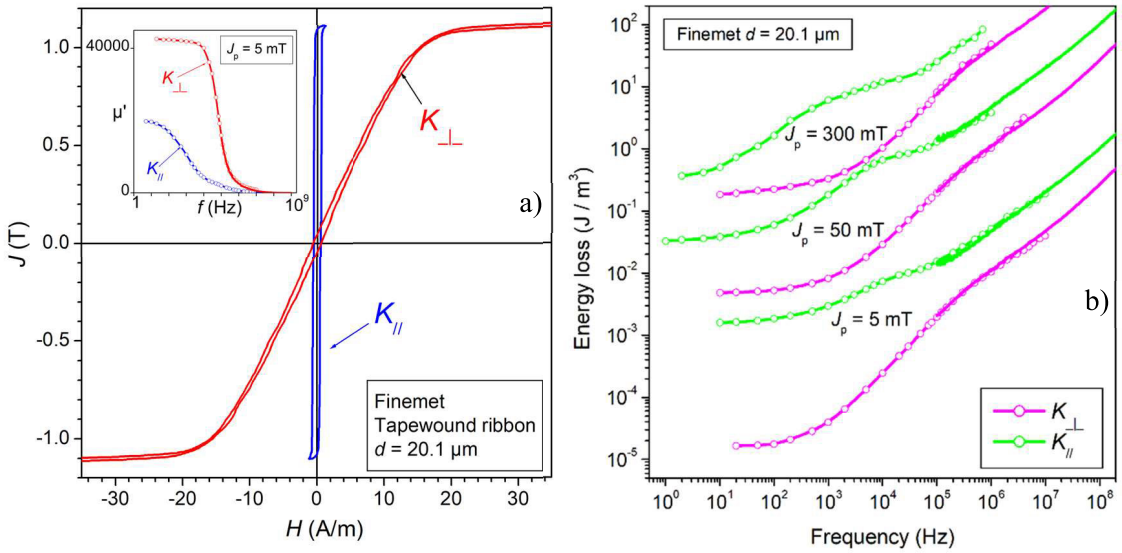

FIGURE 1. a) Quasi-static major hysteresis loops in a 20.1 μm thick tapewound nanocrystalline ribbon subjected to either longitudinal ($K_{//}$) or transverse ($K_{\perp}$) field annealing. The inset shows the frequency dependence of the associated initial permeabilities $\mu'(f)$ (peak polarization $J_p = 5$ mT). b) Corresponding broadband energy loss behavior measured at three different J_p values. The dramatic decrease of the loss following the passage from the ($K_{//}$) to the ($K_{\perp}$) ribbons marks the transition from domain wall dominated ($K_{//}$) to rotation dominated ($K_{\perp}$) magnetization process.

high electrical resistivity, a unique property, conducive to low loss and high permeability across a broad frequency range. These properties compound with solidly established material processing and low cost. However, the operating conditions of many devices, possibly subjected to wide temperature excursions and complex excitation regimes, and the desired minimum volume of the inductive components, make nanocrystalline and amorphous cores an attractive option [10], [11], [12]. The Co-based amorphous and the nanocrystalline Finemet-type ribbons are endowed with vanishing magnetocrystalline and magnetostrictive anisotropies, with ensuing extra-soft magnetic behavior. Property tailoring by field annealing, low and weakly temperature-dependent power losses, and saturation magnetization largely increased with respect to the Mn-Zn and Ni-Zn ferrites, are among the appealing features of these alloys [13], [14], [15]. Theory and experiments show that the nanocrystallized Finemet ($Fe_{73}Nb_3Cu_1Si_{16}B_7$) alloys are affected by a residual random anisotropy $K_0 \sim 2$ - 4 J/m^3, which becomes negligible ($K_0 \sim$ some 10^{-3} J/m^3) in the Co-based amorphous alloys, according to the degree of atomic short-range order [13]. Consequently, local atomic ordering, guided by a saturating magnetic field at a conveniently high temperature, can generate a macroscopic anisotropy. This is induced colinear with the magnetization during the treatment and can largely overcome the native random anisotropy. Either rectangular or quasi-linear $J(H)$ quasi-static loops are therefore obtained with the saturating field directed either along or transverse to the ribbon length [16], [17]. Different anisotropy values become available and the hysteresis loop shape can be conveniently manipulated through an appropriate time-temperature schedule. This is dramatically manifested by the broad range of near-linear magnetization curves achievable through a sequence of induced transverse anisotropy $K_{\perp}$ values [18].

Transverse anisotropy cores have distinctive merits concerning versatility, linearity, and loss minimization. The example shown in Fig. 1 provides a typical broadband response of a tapewound nanocrystalline Finemet alloy of thickness $d = 20.1$ μm, subjected to either longitudinal ($K_{//}$) or transverse ($K_{\perp}$) field annealing. The dramatic decrease of the quasi-static and AC energy loss in the $K_{\perp}$ samples and the corresponding well-defined permeability value, nearly constant over a wide frequency range, make the so-treated cores highly appealing to applications. Profuse applicative examples are found in power electronics (e.g., high-frequency transformers, common mode inductors, magnetic amplifiers, chokes), as well as earth leakage breakers and current transformers [18], [19], [20], [21]. Whatever the case, the wideband loss behavior sketched in Fig. 1 is not prone to a simple quantitative interpretation. A typical shortcut in dealing with this complex phenomenology is offered by Steinmetz's equation and its many versions [5], [22], [23]. These have the obvious drawback of a tenuous physical justification, which translates into adjustable parameters, the lower their number, the higher the adjustments to be made under varying operating conditions. By looking at the problem from an exclusively phenomenological viewpoint, the loss surface model offers a solution, via the creation of an archive of field values $H(B, dB/dt)$ by appropriately extended measurements under a regime of triangular induction $B(t)$ [24]. After separate calculation and subtraction

of the hysteresis contribution, the dynamic response of the material for a generic dB/dt regime can be reconstructed by interpolation on the field surface $H_{\rm dyn}(B,\ {\rm d}B/{\rm d}t)$. Aiming, however, at a physically grounded approach, one can find a comprehensive tool in the Statistical Theory of Losses (STL) [25]. This has been shown to apply to the loss versus frequency dependence in both longitudinal and transverse anisotropy alloys, at least in terms of elementary loss decomposition [14], [16], [17], [26], at low and intermediate frequencies (up to 10 - 50 kHz). It is remarked, however, that, depending on treatment, the good soft magnetic response of the material can go far beyond such frequency limits. It is observed in Fig. 1a, for example, that the transverse anisotropy nanocrystalline ribbon can exhibit significant values of the initial permeability at 1 MHz ($\mu' \sim$ 3000), 10 MHz ($\mu' \sim$ 600), and 100 MHz ($\mu' \sim$ 65). There is no simple way to justify and predict the behavior of permeability and energy loss across such an extended frequency range. Skin effect, resonances, spin damping, exchange field, anisotropy and eddy current fields, all play a role in the magnetization process and can affect the energy dissipation at very high frequencies. Consequently, an evolutionary adaptation of the STL is required, to connect low- and high-frequency predicting strategies. We show in this work that such an objective can be achieved by analytical methods in the highly efficient $K_{\_|\_}$ alloys, where the homogenous character of the rotations, always predominant with respect to the domain wall (dw) displacements, makes them naturally prone to a description by Maxwell's diffusion equation. The dynamic evolution of the magnetic constitutive equation of the material is taken into account by the Landau-Lifshitz equation [27], [28], [29], [30]. The experiments are carried out from DC to 1 GHz on tapewound $K_{\_|\_}$ nanocrystalline and Co-based amorphous ribbons of different thickness (6.1 μm $\leq d \leq$ 25 μm) and different induced transverse anisotropy (7.0 J/m^3 $\leq K_{\_|\_} \leq$ 251 J/m^3). The magnetic measurements, performed by fluxmetric and transmission line methods, are supported by observations of the dw dynamics by Kerr stroboscopy. The fitting of the rotational loss and the ensuing decomposition of the measured loss are obtained by identifying the exchange length, the Landau-Lifshitz damping constant, and the effective out-of-plane demagnetizing coefficient.

II. EXPERIMENTAL PROCEDURE

This Section summarises the preparation and characterization methods of several nanocrystalline and amorphous ribbons subjected to anisotropy-inducing thermomagnetic treatments. Dynamic magneto-optical domain observations supplement the magnetic characterization.

$Fe_{73}Nb_3Cu_1Si_{16}B_7$, $Co_{67}Fe_4B_{14.5}Si_{14.5}$, and $Co_{71}Fe_4B_{15}Si_{10}$ amorphous ribbons of thickness 15 – 25 μm and width 5 – 10 mm were prepared by Planar Flow Casting, loosely wound inside a boron nitride case (5 – 10 layers) of diameter 18 mm, and subjected to thermal treatment under a saturating 15 kA/m transverse field. Before the thermal treatment, a few ribbons were thinned by chemical etching, down to a minimum thickness $d = 6.1$ μm (amorphous alloys) and $d = 13$ μm (Finemet). The so-made thickness reduction caused, in general, some deterioration of the quasi-static magnetic properties, more than compensated by a decrease of the loss at high frequencies. Companion samples were treated under a circumferential field $H_{//} \sim$ 500 A/m, sufficient to saturate the material in the longitudinal direction. With the field applied from the beginning to end of the thermal cycle, the precursor $Fe_{73}Nb_3Cu_1Si_{16}B_7$ alloy was brought to 550 °C, to achieve the nanocrystalline structure (two-hour stay in vacuum atmosphere), and slowly cooled to room temperature. The amorphous Co-based alloys were stress-relaxed at 350 °C and cooled, with an intermediate field-annealing step of a few hours at 280 °C – 250 °C. Reproducible magnetothermal treatments were the natural outcome of a vast repertoire of treatments performed over the years in the INRIM lab.

The DC and AC fluxmetric magnetic characterization of the so-treated ring samples was performed, across the polarization range 2 mT $\leq J_{\rm p} \leq$ 500 mT, up to a few MHz at $T = 23 \pm 1$ °C. A calibrated digital hysteresisgraph-wattmeter, endowed with the DC-10 MHz HSA 4101 power amplifier and the 350 MHz, 2.5 GS/s TDS5034 oscilloscope, was employed. The primary and secondary winding arrangements (0.2 mm wire diameter) evolved with the measuring frequency, to minimize the role of the stray parameters. To cope with the relevant soft magnetic response displayed by these alloys at very high frequencies, transmission line measurements in reflection and sweep mode were made from a few hundred kHz to 1 GHz, by means of a VNA analyzer (Rohde & Schwarz mod. ZNB8, 10 mW incident power). This measuring approach is described in [31]. As anticipated by the results shown Fig. 1 and discussed in the following, the actual VNA results on high-frequency permeability and energy loss can be extrapolated to a defined $J_{\rm p}$ value, in excellent agreement with the fluxmetrically measured quantities over the shared frequency interval. The setups are calibrated according to the established INRIM traceability programs. The uncertainty is estimated to range, according to the scheme discussed in [31], between ± 3 % (intermediate f and $J_{\rm p}$ values) and ± 8% (lowest f and $J_{\rm p}$ values and frequencies higher than 100 MHz).

The dynamics of the domain walls was directly observed on polished strip samples, subjected to the same magnetothermal treatment carried out on the ring samples. A fast magneto-optic Kerr stroboscopic setup was employed, composed of a wide-field microscope (Zeiss Axioscop 2 Plus) and a gated intensified charge-coupled device (CCD) camera (Picostar LaVision). Given the extreme brittleness of the nanocrystalline strips, the Kerr experiments were reserved to the amorphous Co-based alloys. Kerr and fluxmetric measurements were performed on single strip samples, placed between the pole faces of a Mn-Zn ferrite U-core, up to 1 MHz. A detailed description of the Kerr setup and the related measuring procedure is given in [32].

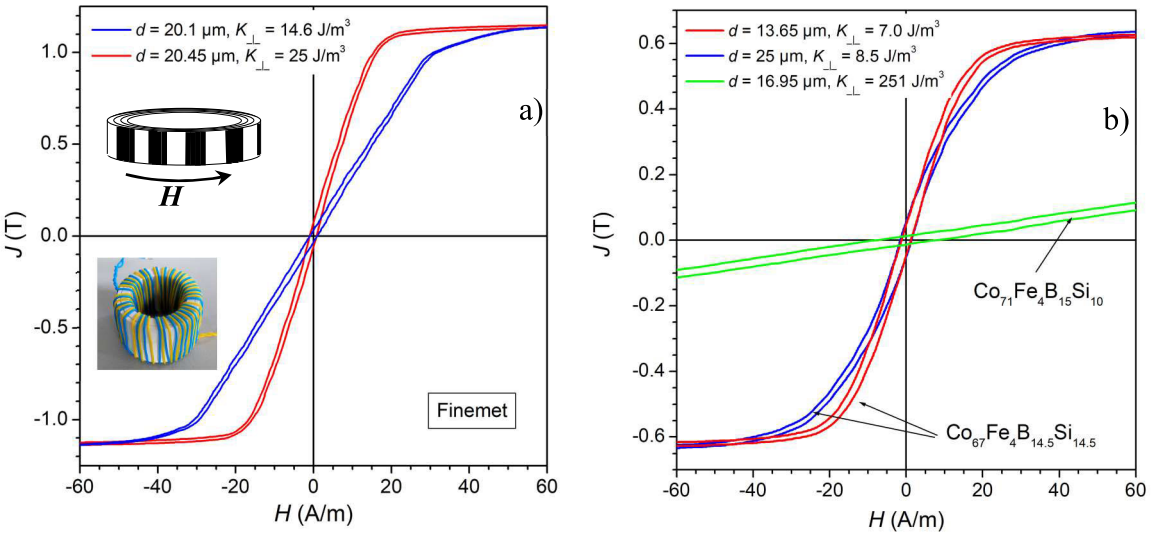

FIGURE 2. Major quasi-static hysteresis loops obtained in nanocrystalline (a) and amorphous (b) tapewound ring samples (see Table 1). They have been subjected to different thermal treatments under a transverse saturating magnetic field, resulting in different values of the transverse induced anisotropy $K_{\perp}$ and a quasi-linear $J(H)$ behavior. The transverse domain structure is sketched in the inset.

TABLE 1. Physical and magnetic parameters of the investigated transverse anisotropy nanocrystalline (Finemet) and amorphous ribbons. They are treated and measured as 18 mm diameter tapewound ring samples. $d \equiv$ ribbon thickness; $J_s \equiv$ saturation polarization; $\rho \equiv$ electrical resistivity; $K_{\perp} \equiv$ transverse anisotropy constant; $l_e \equiv$ exchange length; $f_0 \equiv$ predicted resonance frequency; $f_1 \equiv$ predicted relaxation frequency; $\alpha \equiv$ Landau-Lifshitz damping constant; $N_{dz} \equiv$ effective demagnetizing coefficient normal to the ribbon plane.

Composition	Structure	d (μm)	J_s (T)	ρ (Ω m)	$K_{\perp}$ (J/m^3)	l_e (nm)	f_0 (MHz)	f_1 (MHz)	α	N_{dz}
$Fe_{73}Nb_3Cu_1Si_{16}B_7$	Nanocryst.	12.90	1.25	$118\cdot10^{-8}$	28	35.2	80.3	7.55	0.2	0.13
$Fe_{73}Nb_3Cu_1Si_{16}B_7$	Nanocryst.	20.10	1.25	$118\cdot10^{-8}$	14.6	15	110.5	15.6	0.054	0.42
$Fe_{73}Nb_3Cu_1Si_{16}B_7$	Nanocryst.	20.45	1.25	$118\cdot10^{-8}$	25	15.9	125	20.6	0.07	0.32
$Co_{67}Fe_4B_{14.5}Si_{14.5}$	Amorphous	6.1	0.65	$141\cdot10^{-8}$	9.3	68	133	6.28	0.161	0.98
$Co_{67}Fe_4B_{14.5}Si_{14.5}$	Amorphous	13.65	0.65	$141\cdot10^{-8}$	7.0	52	66.6	5.98	0.13	0.31
$Co_{67}Fe_4B_{14.5}Si_{14.5}$	Amorphous	25.0	0.65	$141\cdot10^{-8}$	8.5	39	86	14.7	0.06	0.45
$Co_{71}Fe_4B_{15}Si_{10}$	Amorphous	16.95	0.89	$124\cdot10^{-8}$	251	44	632	332	0.054	0.87

III. MAGNETIZATION ROTATIONS vs. DOMAIN WALL DISPLACEMENTS

Field-annealed amorphous and nanocrystalline alloys are endowed with uniform induced anisotropy (either $K_{//}$ or $K_{\perp}$) and generally much lower residual random anisotropy δK. The resulting domain structure is therefore made of a rather sharp slab-like array of antiparallel domains separated by 180° dws, either longitudinally ($K_{//}$) or transversally ($K_{\perp}$) directed. Treatments leading to very low induced anisotropy (few J/m^3), comparable with δK, lead to a somewhat irregular domain pattern [16]. We deal here with the transverse anisotropy materials, where $K_{\perp}$ ranges between 7 and 250 J/m^3. These materials exhibit minimum energy loss and wideband response, as put in evidence by the example shown in Fig. 1. They are listed in Table 1, together with their physical and magnetic parameters. Fig. 2 provides an overview of the quasi-static major hysteresis loops obtained in representative samples.

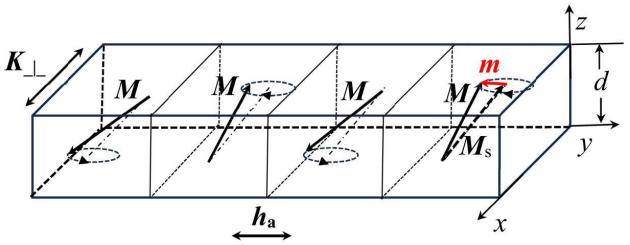

FIGURE 3. Ideal domain configuration and rotational-precessional magnetization mode in transverse anisotropy nanocrystalline/amorphous ribbons (not in scale) under the applied AC field h_a. The precessional trajectory of the oscillating M vector is a flattened ellipse. The local $m_z(t)$ component is made negligible at all frequencies, compared to the measured longitudinal component $m_y(t)$, by the high value of the demagnetizing coefficient N_{dz}.

The ideal response of a transverse domain structure to an alternating longitudinal field is sketched in Fig. 3. With the longitudinally applied AC field h_a, the 180° dws are still and

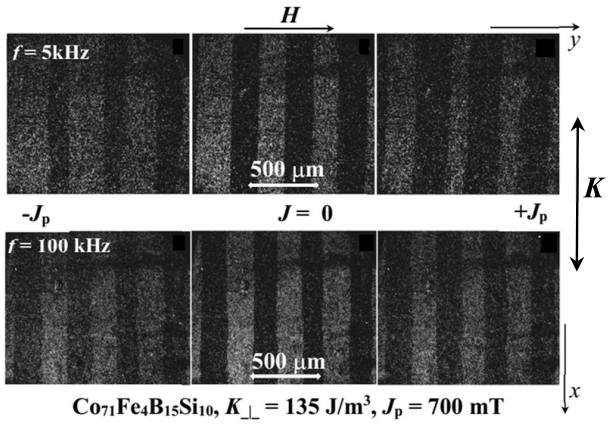

FIGURE 4. Domain structure in amorphous ribbons $Co_{71}Fe_4B_{15}Si_{10}$ annealed under transverse saturating field ($K_{\perp} = 135$ J/m^3). It is observed by the stroboscopic Kerr method at 5 kHz and 100 kHz. The images refer to the tips J_p of the hysteresis loop taken between ±700 mT and to the passage through $J = 0$. The loss of contrast at $\pm J_p$ stems from the partially rotated magnetization (longitudinal field H_a). The domain wall displacements accompanying rotations are hindered by dissipation on passing from 5 kHz to 100 kHz.

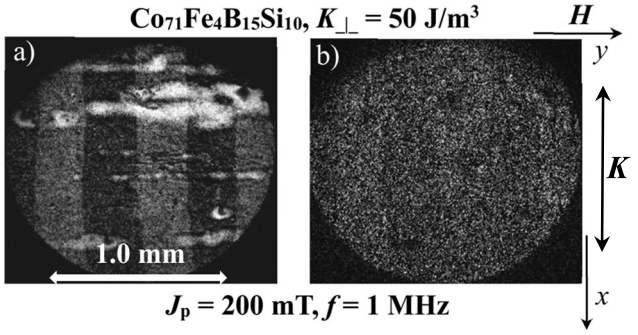

FIGURE 5. The domain walls in the $K_{\perp}$ $Co_{71}Fe_4B_{15}Si_{10}$ amorphous ribbon ($d = 19\mu$m) are definitely at rest at 1 MHz. a) Domains at the tip of the loop taken at $+J_p = 200$mT. b) The image taken at $-J_p$ is subtracted from a). Faint traces of the domains, signaling the rotation of the magnetization between ±200mT and a scant dw motion, are observed.

the magnetization $\boldsymbol{M}$, precessing around the anisotropy field H_k inside the domains, follows a flattened elliptical trajectory, while maintaining pole-free dws. It is shown that the local component $m_z(t)$ normal to the ribbon plane is always orders of magnitude lower than the longitudinal component $m_y(t)$ and any dissipative effect related to it can be neglected. We realize in this ideal case the condition for the fully homogeneous and reversible, scale-independent, magnetization process, leading to the so-called dynamic classical losses, the lowest attainable loss limit. The experiments and the theoretical treatment discussed in this work show that such a limit is actually approached beyond 100 kHz – 1 MHz, depending on J_p and the ribbon thickness. It is apparent that, even in the presence of a sharp transverse domain structure, dw motion persists, thereby justifying the existence of a finite value of the quasi-static (hysteresis) loss W_{hyst}. The Kerr observations show that the transversally directed 180° dws oscillate under the longitudinal AC field [32]. However, it is additionally observed that the net magnetization variation along the transverse direction x is negligible, implying that the dw motion is the result of a mere rearrangement of the domain spacing caused by the magnetostatic energy at the ribbon edges, continuously changing with the rotations [33]. The Kerr images in Fig. 4 show an example of changing domain pattern coexisting with magnetization rotations in a $Co_{71}Fe_4B_{15}Si_{10}$ ribbon endowed with a transverse $K_{\perp} = 135$ J/m^3, cycled between $\pm J_p = 700$ mT at 5 kHz and 100 kHz. A loss of contrast appears at the tip points of the loop, compared to the image at $J = 0$. It is associated with the rotation made by the magnetization on passing from the demagnetized state to $\pm J_p$. It is further apparent that the dw activity observed at 5 kHz is much more hindered at 100 kHz, for the same J_p value. The images shown in Fig. 5, taken on a similar sample ($K_{\perp} = 50$ J/m^3) at the tip points $\pm J_p = 200$ mT of a loop measured at 1 MHz, show that the dws are motionless at this frequency, where only rotations occur. The parasitic torque acting on the rotating magnetic moments, proportional to the spin angular velocity, is, in fact, more effective in restraining the rotation inside the dws than inside the domains. We conclude that the combination of distinguishable dw processes and rotations makes the broadband loss phenomenology consistent with the basic concept of loss decomposition, with the contribution by rotations inside the domains lumped in the classical component $W_{rot} \equiv W_{class}$. It is easily realized, according to the scheme of Fig. 3, that the eddy current paths form a continuum in the cross-section and along the ribbon length.

IV. A MODEL FOR THE ROTATIONAL LOSS

We demonstrate in this Section that the broadband energy losses associated with the rotational magnetization process can be calculated by closed formulas. To this end, we derive the magnetic constitutive equation via the Landau-Lifshitz equation, to be coupled with Maxwell's diffusion equation. This contrasts with the standard approach to the classical energy loss in magnetic steel sheets, where an analytical solution is found for the Maxwell diffusion equation in a homogeneous material endowed with defined DC permeability μ_{DC} [25]. The character of the magnetization process taking place in these $K_{\perp}$ materials, as induced by the Kerr observations, and the quasi-linear behavior of the magnetization curves (Fig. 2), makes plausible in principle the identification of the magnetic constitutive equation of the alloys with μ_{DC}. By doing so, we obtain the standard formula for the classical eddy current loss at peak induction B_p versus frequency f in a sheet of conductivity σ [Ω^{-1}m^{-1}] and thickness d [m]

$$W_{class,\mu DC}(B_p, f) = \frac{\pi}{2}\frac{B_p^2}{\mu_{DC}}\frac{\sinh\eta - \sin\eta}{\cosh\eta - \cos\eta}, \left[\mathrm{J/m^3}\right] \quad (1)$$

where $\eta = \sqrt{\pi\sigma\mu_{DC}d^2 f}$. The dimensionless parameter η provides a measure of the flux penetration, the higher the η value, the lower the penetration depth (skin effect). For

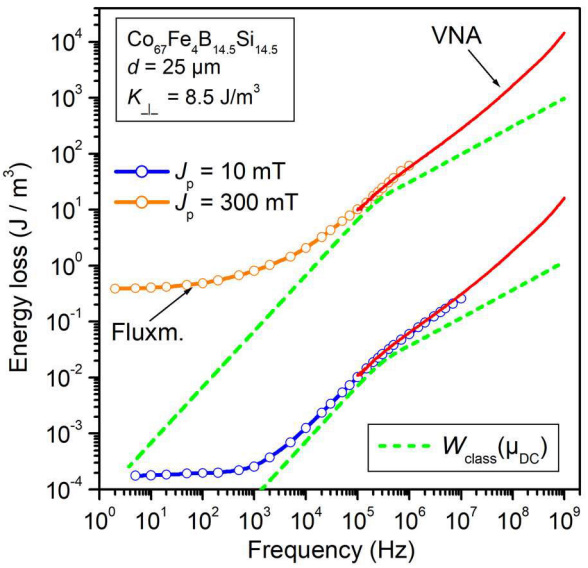

FIGURE 6. The energy loss measured at two largely different peak polarization values in a $Co_6Fe_4\ B_{14.5}Si_{14.5}$ amorphous ribbon ($K_{\perp} = 8.5$ J/m^3, $d = 25\mu$m) is compared with the classical loss W_{class} (μDc) predicted according to the standard Eq. (1). The magnetic constitutive equation is identified in this case with the DC permeability ($\mu_{rDC} = 20130$ at $J_p = 10$ mT, $\mu_{rDC} = 24000$ at $J_p = 300$ mT).

$\eta < 2$, the flux uniformity across the sheet thickness is ensured and (1) reduces to

$$W_{\text{class},\mu_{DC}}(B_p, f) = \frac{\pi^2}{6}\sigma B_p^2 d^2 f \left[\text{J/m}^3\right]. \tag{2}$$

We shall assume here and in the following $B_p \equiv J_p$. We therefore provide in Fig. 6 an illustrative example, where the prediction by (1) is associated with the experimental $W(f)$, measured over the broad 1 Hz - 1GHz frequency range in the $Co_{67}Fe_4B_{14.5}Si_{14.5}$ ribbon ($K_{\perp} = 8.5$ J/m^3, $d = 25\ \mu$m). The calculated $W_{\text{class},\mu_{DC}}(f)$ is largely deficient with respect to $W(f)$ below about 100 kHz – 1 MHz. Here the dissipation descends from the eddy currents enwrapping the moving dws and one can thus identify a loss contribution $W_{dw}(f) = W_{hyst} + W_{exc}(f)$, the sum of the hysteresis and excess components, eventually fading out at very high frequencies. The change of slope of $W_{\text{class},\mu_{DC}}(f)$ from f to $f^{1/2}$ predicted by (1) upon entering the MHz range follows from the increase of the parameter η to the point where the skin depth becomes approximately lower than $d/3$. This appears also to be the frequency neighborhood of waning $W_{dw}(f)$. We are thus confronted at these frequencies with a state of uniform rotational process, emulating the behavior of a saturated material and complying in principle with the predicted $W_{\text{class},\mu_{DC}}(f)$. However, the predicted diverging trends of the measured $W(f)$ and $W_{\text{class},\mu_{DC}}(f)$) in the upper frequency range demonstrate that a quasi-static constitutive equation is not compatible with the material response, where the time scales of spin dynamics and electromagnetic excitation become comparable. For the relatively simple character of the magnetization process in the $K_{\perp}$ alloys, a solution of the Landau-Lifshitz equation for the dynamics of the magnetization $\boldsymbol{M}$ is expected to apply [27]

$$\frac{d\boldsymbol{M}}{dt} = -\gamma\mu_0\,\boldsymbol{M}\times\boldsymbol{H}_{\text{eff}} + \frac{\alpha}{M_s}\,\boldsymbol{M}\times\frac{d\boldsymbol{M}}{dt}, \tag{3}$$

where $\boldsymbol{H}_{\text{eff}}$ is the effective field, $\gamma = 1.76 \times 10^{11}$ (T^{-1} s^{-1}) is the electron gyromagnetic ratio, α is the Landau-Lifshitz damping constant, and M_s is the saturation magnetization.

At equilibrium, under a zero applied field, the magnetization in each domain is directed along the transverse direction x, therefore $\boldsymbol{M} = \boldsymbol{M}_s = M_s\cdot\hat{\mathbf{e}}_x$ and $\boldsymbol{H}_{\text{eff}} = \boldsymbol{H}_k = (2K_{\perp}/\mu_0 M_s)\cdot\hat{\mathbf{e}}_x$. Consequently, Eq. (3) reduces to $\boldsymbol{M}_s \times \boldsymbol{H}_k = \mathbf{0}$.

Under a y-directed AC field $\boldsymbol{h}_a$, a scheme for the precession of $\boldsymbol{M}$ is sketched in Fig. 3, where $\boldsymbol{M} = \boldsymbol{M}_s + \boldsymbol{m}$ and $\boldsymbol{m}$ is the dynamic magnetization. The effective field $\boldsymbol{H}_{\text{eff}}$ becomes the vector composition of the static anisotropy field $\boldsymbol{H}_k$, the applied AC field $\boldsymbol{h}_a$, and all the dynamic fields accompanying the spin precessional motion. Therefore $\boldsymbol{H}_{\text{eff}} = \boldsymbol{H}_k + \boldsymbol{h}_{\text{eff}}$, where $\boldsymbol{h}_{\text{eff}}$ lumps the resultant dynamic fields. Under small oscillations ($|\boldsymbol{h}_a| \ll |\boldsymbol{H}_k|$, $|\boldsymbol{m}| \ll |\boldsymbol{M}|$) Eq. (3) can be linearised and under harmonic regime it simplifies into

$$j\omega\boldsymbol{m} = -\gamma\mu_0\,(\boldsymbol{m}\times\boldsymbol{H}_k + \boldsymbol{M}_s\times\boldsymbol{h}_{\text{eff}}) + \frac{\alpha}{M_s}\boldsymbol{M}_s\times j\omega\boldsymbol{m}, \tag{4}$$

By separating the components along the y and z directions, we get the scalar relationships between the effective field and the magnetization components

$$\begin{pmatrix} h_{\text{eff,y}} \\ h_{\text{eff,z}} \end{pmatrix} = \begin{pmatrix} h_0 + j\frac{\omega}{\gamma\mu_0 M_s}\alpha & -j\frac{\omega}{\gamma\mu_0 M_s} \\ j\frac{\omega}{\gamma\mu_0 M_s} & h_0 + j\frac{\omega}{\gamma\mu_0 M_s}\alpha \end{pmatrix} \tag{5}$$

where $h_0 = \frac{H_k}{M_s}$ is an a-dimensional parameter.

We synthetically illustrate in the following the calculations leading to analytical expressions for the complex permeability and energy loss in terms of the physical parameters involved in the rotational processes. The mathematical details are provided in Appendix A. We find the susceptibility $\chi(\omega) = \frac{m_y}{h_{\text{eff,y}}}$ by (5), taking into account the role of the dynamic demagnetizing field normal to the ribbon surface, arising during the precession of $\boldsymbol{M}$. We pose $h_{\text{eff,z}} = -N_{dz}m_z$, with N_{dz} the demagnetizing coefficient. It is always $N_{dz} < 1$, because of the presence of a domain structure, that is, a distribution of polar charges of alternating sign at the ribbon surface. Besides predicting that the normal component m_z is related to the longitudinal component m_y by the equation

$$m_z = -j\frac{\omega}{\gamma\mu_0 M_s}\frac{1}{\left(h_0 + N_{dz} + j\frac{\omega}{\gamma\mu_0 M_s}\alpha\right)}m_y \tag{6}$$

we obtain by (5) the complex susceptibility

$$\chi(\omega) = \frac{m_y}{h_{\text{eff,y}}} = \left(h_0 + j\frac{\omega}{\gamma\mu_0 M_s}\alpha - \left(\frac{\omega}{\gamma\mu_0 M_s}\right)^2 \frac{1}{\left(h_0 + N_{dz} + j\frac{\omega}{\gamma\mu_0 M_s}\alpha\right)}\right)^{-1} \tag{7}$$

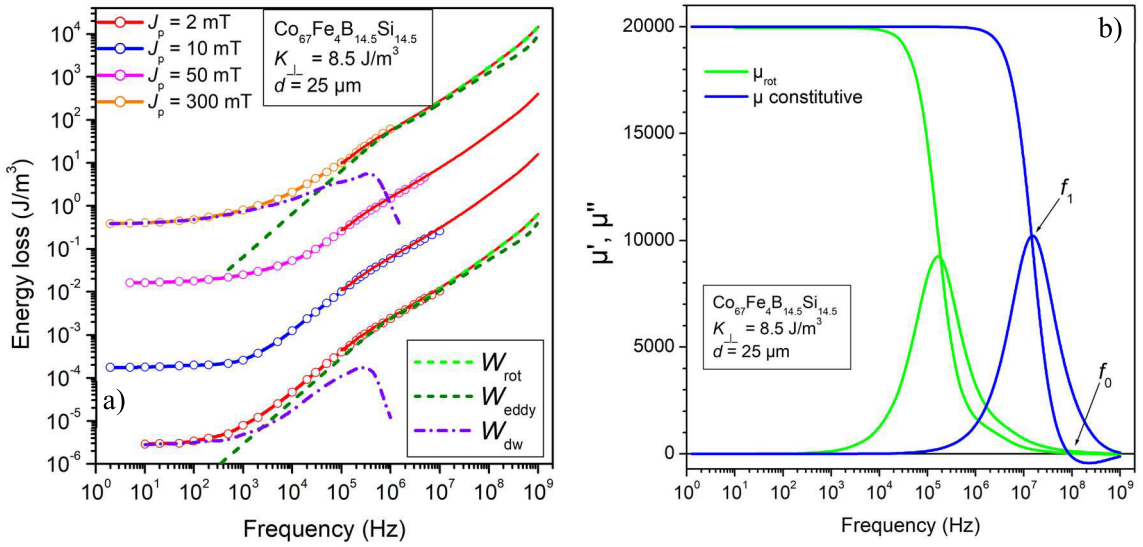

FIGURE 7. a) Frequency dependence of the energy loss $W(f)$ measured in the $Co_{67}Fe_4B_{14.5}Si_{14.5}$ amorphous ribbon of Fig. 6 up to $J_p = 300$ mT ($J_p \sim 0.45\ J_s$) and the related prediction by (19) of the classical loss $W_{rot}(f)$ Fitting parameters: $\alpha = 0.06$; $N_{dz} = 0.45$; $l_e = 39$ nm. The dissipative contribution due to eddy currents $W_{eddy}(f) = W_{rot}(f) - W_{sd}(f)$ is discriminated against the spin damping term $W_{sd}(f)$, whose role can be appreciated beyond about 10 MHz, where $W_{rot}(f)$ and $W_{eddy}(f)$ tend to bifurcate. The energy loss $W_{dw}(f) = W(f) - W_{rot}(f)$ associated with the motion of the dws is further put in evidence and found to drop on approaching the MHz range, as anticipated by the Kerr observations. b) The complex magnetic constitutive equation, identified with (12), is shown in association with the complex permeability predicted by (18). The cutoff at the frequency f_1 shows that relaxation largely predates, in this and all the other tested samples, the resonance, occurring at the frequency f_0.

After some manipulations of (7), $\chi(\omega)$ can be written as

$$\chi(\omega) = \frac{\chi_{DC}\left(1 + j\frac{\omega}{\omega_2}\right)}{1 - \left(\frac{\omega}{\omega_0}\right)^2 + j\left(\frac{\omega}{\omega_1}\right)} \tag{8}$$

where $\chi_{DC} = 1/h_0$ and

$$\omega_0 = \left(\frac{h_0\,(h_0 + N_{dz})}{1+\alpha^2}\right)^{1/2} \cdot \gamma\mu_0 M_s, \tag{9}$$

$$\omega_1 = \frac{1}{\alpha}\frac{h_0\,(h_0 + N_{dz})}{2h_0 + N_{dz}} \cdot \gamma\mu_0 M_s, \tag{10}$$

and

$$\omega_2 = \frac{1}{\alpha}(h_0 + N_{dz}) \cdot \gamma\mu_0 M_s \tag{11}$$

It is found that, within the envisaged span covered by the α, χ_{DC}, and N_{dz} values, $\omega_2 \sim 10^{11}$-10^{12} s^{-1} and $\omega/\omega_2 \ll 1$ across the whole experimental frequency range. Consequently, $\chi(\omega)$ reduces to the classical equation of the forced oscillator

$$\chi(\omega) = \frac{m_y}{h_{eff,y}} = \frac{\chi_{DC}}{1 - \left(\frac{\omega}{\omega_0}\right)^2 + j\left(\frac{\omega}{\omega_1}\right)}, \tag{12}$$

where ω_0 and ω_1 are the resonance and relaxation frequencies, respectively.

We are now in a position to perform the electromagnetic analysis by coupling the constitutive equation (12) to Maxwell's diffusion equation, governing the magnetization profile along the coordinate z, ranging between $\pm\, d/2$.

$$\frac{\partial^2 h_y}{\partial z^2} = j\omega\sigma b_y = j\omega\sigma\mu_0\left(m_y + h_y\right), \tag{13}$$

where σ is the alloy conductivity. In this equation, $b_y = \mu_0\left(m_y + h_y\right)$ is the flux density, and h_y is the *Maxwellian* field. At sufficiently high frequencies, the eddy current counterfield hinders the spin rotation at the ribbon core, an effect contrasted by the torque of the exchange field $h_{ey} = l_e^2 \cdot \partial^2 m_y/\partial z^2$, which tends to maintain parallel the adjacent spins. m_y will thus depend on $h_{eff,y} = h_y + h_{ey}$, according to

$$m_y(z) = \chi(\omega) \cdot \left(h_y(z) + l_e^2\frac{\partial^2 m_y}{\partial z^2}\right), \tag{14}$$

where the exchange length is of the order of $l_e = \sqrt{2A\mu_o}/J_s^2$, with A [J/m] the stiffness constant. Solution of the coupled Eqs. (13) and (14) is obtained according to the appropriate boundary conditions, as discussed in full detail in Appendix A. It provides a closed expression for the field $h_y(z)$

$$h_y(z) = C_1\frac{\cosh(\lambda_1 z)}{\sinh\left(\lambda_1 d/2\right)} + C_2\frac{\cosh(\lambda_2 z)}{\sinh\left(\lambda_2 d/2\right)}, \tag{15}$$

where λ_1 and λ_2 are solutions of the biquadratic algebraic equation

$$\chi(\omega)\, l_e^2\lambda^4 - \left(1 + j\omega\sigma\mu_0\chi(\omega)\, l_e^2\right)\lambda^2 + \\ + j\omega\sigma\mu_0\left(1 + \chi(\omega)\right) = 0, \tag{16}$$

and the constants C_1 and C_2 are obtained by imposing the boundary conditions $\left.\frac{\partial h_y}{\partial z}\right|_{z=d/2} = j\omega\sigma B_p d/2$ and $\left.\frac{\partial^3 h_y}{\partial z^3}\right|_{z=d/2} = -\omega^2\sigma^2\mu_0 B_p d/2$.

The applied field coincides with h_y at the sheet surface

$$h_a = h_y\left(d/2\right) = C_1\coth\left(\lambda_1 d/2\right) + C_2\coth\left(\lambda_2 d/2\right) \tag{17}$$

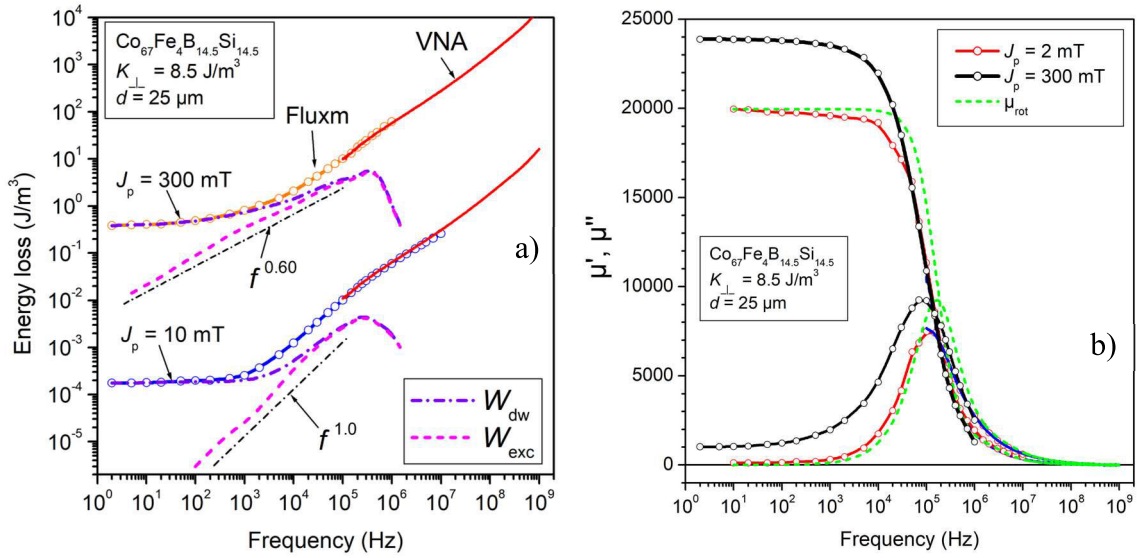

FIGURE 8. a) The hysteresis loss component $W_{hyst} = \lim_{f \to 0} W(f)$ and the dynamic excess component $W_{exc}(f)$ in the $Co_{67}Fe_4B_{14.5}Si_{14.5}$ amorphous ribbon are extracted from the $W(f)$ curves shown in Fig. 7a after subtraction of $W_{rot}(f)$. The $W_{dw}(f) = W_{hyst} + W_{exc}(f)$ contribution falls down beyond a few hundred kHz, consistent with the freezing of the dw motion observed by the magneto-optical experiments. $W_{exc}(f)$ follows, before its downturn at high frequencies, the power law $W_{exc}(f) \propto f^n$, with $0.5 \le n \le 1$. b) The dashed lines represent the rotational permeability μ_{rot} predicted by (18). The experimental μ' and μ'' taken at $J_p = 2$ mT show earlier relaxation, on account of the dissipation by the moving dws. These provide some extra-contribution to μ at low frequencies and high J_p values (e.g., $J_p = 300$ mT). However, high- and low- J_p curves all merge at high frequencies.

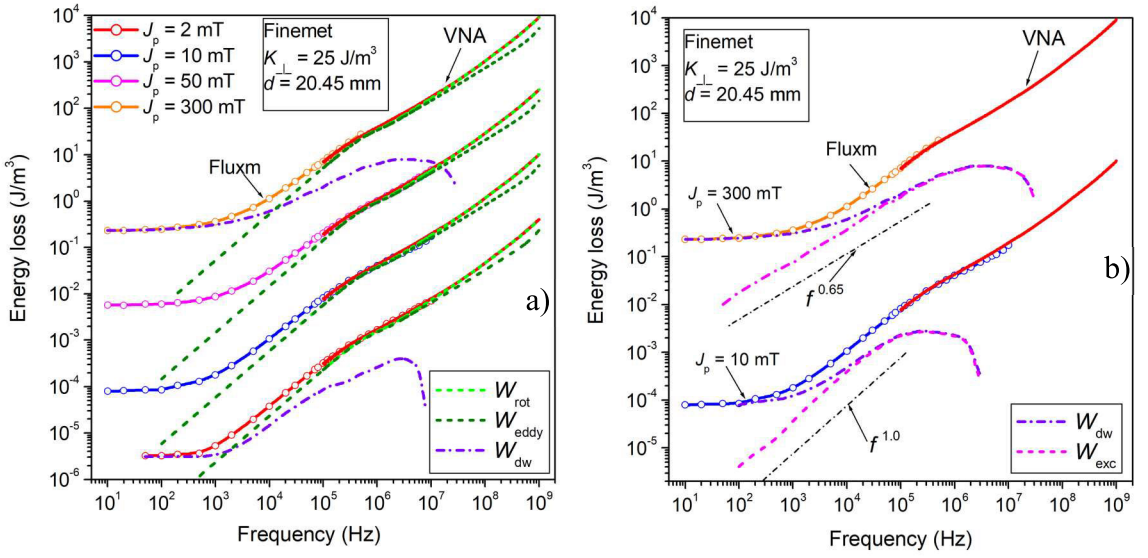

FIGURE 9. a) As in Fig. 7 a for the 20.45μm thick Finemet ribbon $\left(K_{\perp} = 25\ \mathrm{J/m^3}\right)$. The fitting parameters for $W_{rot}(f)$ are: $\alpha = 0.07$; $N_{dz} = 0.32$; $l_e = 15.9$ nm. b) The excess loss component $W_{exc}(f)$, extracted from $W_{dw}(f)$, exhibits a same decreasing trend with J_p of the exponent of the power law $W_{exc}(f) \propto f^n$ observed in the previous $Co_{67}Fe_4B_{14.5}Si_{14.5}$ amorphous ribbon (Fig. 8a).

and the measured complex permeability is given

$$\mu(\omega) = \mu'(\omega) - j\mu''(\omega) = \frac{B_p}{\mu_0 h_a(\omega)}, \qquad (18)$$

where B_p is the z-average of the local peak induction $b_y(z)$. The classical (specific) loss by rotations is eventually derived for the given B_p (i.e. J_p) value from the real μ' and imaginary μ'' components of $\mu(\omega)$

$$W_{rot}\left(B_p, \omega\right) = \frac{\pi}{\mu_0} \cdot \frac{\mu''(\omega)}{\mu'^2(\omega) + \mu''^2(\omega)} \cdot B_p^2. \quad [\mathrm{J/m^3}] \quad (19)$$

This equation provides the total rotational loss, a quantity given by the sum of eddy current and spin-damping losses.

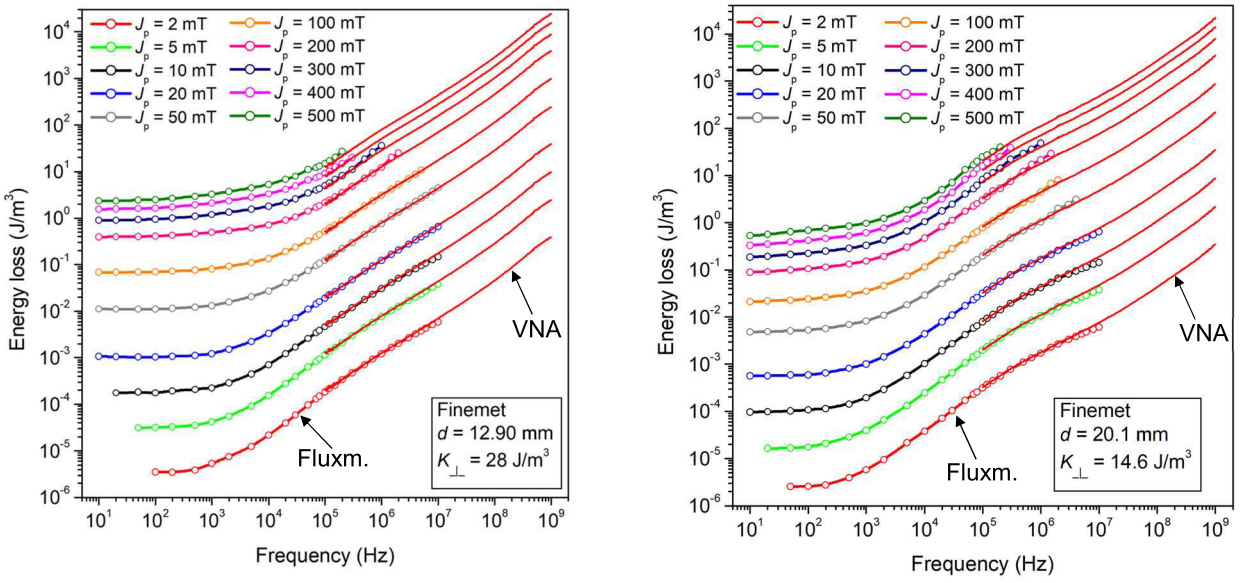

FIGURE 10. Overall $W(f)$ behavior (5 Hz $\leq f \leq$ 1 GHz, 2 mT $\leq J_p \leq$ 500 mT) in Fimenet ribbons of different thickness and different transverse anisotropy values. The fluxmetric and VNA measurements provide overlapping results up to remarkably high J_p values. The slope of the $W(f)$ curves decreases with increasing J_p in the transition region covering the passage from W_{hyst} to W_{rot} (f), consistent with the concurrent decrease of the exponent n of the power law W_{exc} $(f) \propto f^n$ (see Figs. 8a and 9 b).

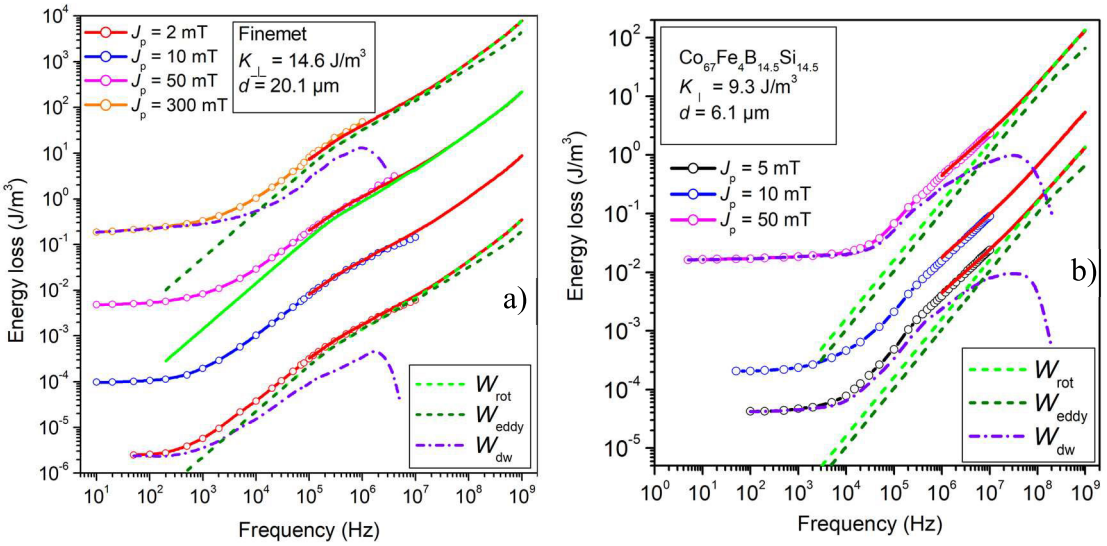

FIGURE 11. a) Loss decomposition in a 20.1μm thick Finemet ribbon $\left(K_{\perp} = 14.6\ \text{J/m}^3\right)$. The fitting parameters for W_{rot} (f) are: $\alpha = 0.054$; $N_{dz} = 0.34$; $l_e = 15$ nm. b) The spin damping component $W_{sd}(f) = W_{rot}$ $(f) - W_{eddy}$ (f) enters into play at low frequencies in the extra-thin $Co_{67}Fe_4B_{14.5}Si_{14.5}$ ribbon($d = 6.1\mu$m). The reduced contribution by W_{eddy} (f) extends the survival of the dw-component $W_{dw}(f)$ up to some 10 MHz.

We shall verify how the amorphous and nanocrystalline materials share these two dissipation phenomena.

V. DC-1 GHz LOSS BEHAVIOR AND ITS ASSESSMENT

We have shown in Fig. 6 that the energy loss $W(f)$ measured up to 1 GHz at two largely different J_p values in a representative transverse $K_{\perp}$ $Co_{67}Fe_4B_{14.5}Si_{14.5}$ amorphous ribbon hardly compares with the prediction of the classical eddy current loss by the standard equation (1) and μ_{DC} as the constitutive equation. Not only did we find the expected trend towards the quasi-static contribution $W_{hyst}(J_p)$ at low frequencies, but also a strong deviation of $W(f)$ with respect to the $f^{1/2}$ dependence predicted to arise by (1), following the surge of the skin effect. Fig. 7a shows that such a large discrepancy can be addressed, in the very same material, by use of the constitutive equation (12) in the calculation of $W_{rot}(f)$ (i.e. $W(f)$ measured at high frequencies) with (19). The values adopted for the parameters involved in the

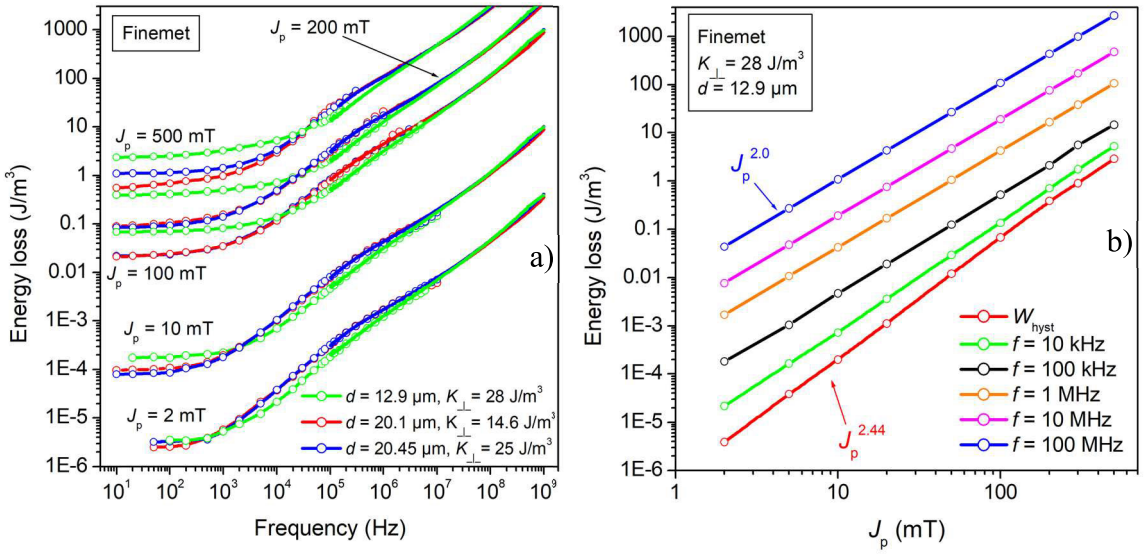

FIGURE 12. a) The quasi-static energy loss in the Finemet alloys increases with the anisotropy value $K_{\perp}$, because it relates to the dw energy, and, to some extent, with thickness reduction, depending on the surface imperfections. Ribbon thinning engenders, however, reduced dynamic losses, eventually compensating for the increase of W_{hyst}. The higher J_p, the higher the frequency at which the compensation takes place, because of the dependence of W_{hyst} on J_p stronger than that of the dynamic loss $W_{dyn}(f)$. We see in fact in (b) that the exponent m in the power law $W(J_p) \propto J_p^m$ decreases from $m = 2.44$ for $W_{hyst}(J_p)$ to $m = 2.0$ at $f \sim 100$ kHz. At very high frequencies, the advantage of thickness is apparently lost in these materials, depending on the specific properties of the magnetic constitutive equation.

prediction by (19) (N_{dz}, α, l_e), consistent with the typical anisotropy values achieved in these materials [16], [17], [18], are listed in Table 1. The presence of the domains enforces a demagnetizing coefficient $N_{dz} < 1$, while the resulting value of the exchange length is compatible with previous assumptions [18]. The associated constitutive function μ is shown in Fig. 7b. To note that the value found for the Landau-Lifshitz damping parameter α is higher than 0.1 in the chemically thinned ribbons. It is remarked also that, in this and all the other cases, the relaxation effect (frequency f_1) largely predates and overcomes resonance (frequency f_0).

The rotational loss $W_{rot}(f) = W_{eddy}(f) + W_{sd}(f)$ is the sum of the dissipative contributions by eddy currents and spin damping, as illustrated in Fig. 7a. $W_{rot}(f)$ coincides with $W_{eddy}(f)$ up to about 10 MHz, where the additional contribution $W_{sd}(f)$ enters into a play, although to a minor extent. $W_{eddy}(f)$ can be discriminated from $W_{rot}(f)$ by calculating the eddy current density phasor $\boldsymbol{j}(z)$, according to $\nabla \times \boldsymbol{H} = \boldsymbol{j}$. With the assumed symmetry we have $j_x(z) = -\frac{dh_y}{dz}$, and using (15) we obtain

$$j_x(z) = \lambda_1 \cdot C_1 \frac{\sinh(\lambda_1 z)}{\sinh\left(\frac{\lambda_1 d}{2}\right)} + \lambda_2 \cdot C_2 \frac{\sinh(\lambda_2 z)}{\sinh\left(\frac{\lambda_2 d}{2}\right)}. \quad (20)$$

$W_{eddy}(f)$ is eventually calculated as

$$W_{eddy}(f) = \frac{1}{fd} \int_{-d/2}^{d/2} \frac{|j_x(z)|^2}{2\sigma} dz \ [\mathrm{J/m^3}] \quad (21)$$

by integration over the z-coordinate.

Having identified the rotational loss, we can retrieve by difference the loss contribution directly ensuing from the motion of the dws $W_{dw}(f) = W(f) - W_{rot}(f)$, in turn composed of a static and a dynamic term $W_{dw}(f) = W_{hyst} + W_{exc}(f)$. We identify in the example of Fig. 8a $W_{hyst} = \lim_{f \to 0} W(f)$ and $W_{exc}(f)$ at two largely different J_p values. The increase of the dw activity under increasing J_p is responsible for the larger than-squared dependence of W_{hyst} on J_p, in contrast with the J_p^2 law predicted and found for $W(f)$ at high frequencies. At the same time, the passage from the low-J_p regime of small dw oscillations to the coarser dw rearrangements at high $J_p$values makes the exponent of the power law $W_{exc}(f) \propto f^n$ to evolve, within the limits $0.5 \leq n \leq 1.0$ envisaged by the theory [25]. We find in Fig. 8a, $n = 1$ at $J_p = 2$ mT and $n = 0.6$ at $J_p = 300$ mT. The latter case tends to conform to the usual scenario contemplated by the STL, where the number N of magnetic objects (MOs) increases with f [34]. The unusual weak field process, where the faint dw displacements are overwhelmed by rotations, fits instead into a picture of constant N. Whatever the case, the dw motion becomes fully superseded by the rotations and $W_{dw}(f)$ drops on approaching the MHz range. This implies that the $\mu'(f)$ and $\mu''(f)$ curves, obtained at different J_p values, eventually collapse on a single curve, as confirmed by the results shown for $J_p = 2$ mT and $J_p = 300$ mT in Fig. 8b, consonant with the found superposition of the experimental VNA and fluxmetric $W(f)$ curves in the appropriate frequency range.

Fig. 9 illustrates the case of loss decomposition in a Finemet ribbon ($d = 20.45$ μm). Again, $W_{rot}(f)$ and $W_{eddy}(f)$ are predicted to coincide up to some 10 MHz, where a minor contribution $W_{sd}(f)$ by spin damping adds to $W_{eddy}(f)$. The $W_{exc}(f) \propto f^n$ dependence, with n decreasing if J_p is increased,

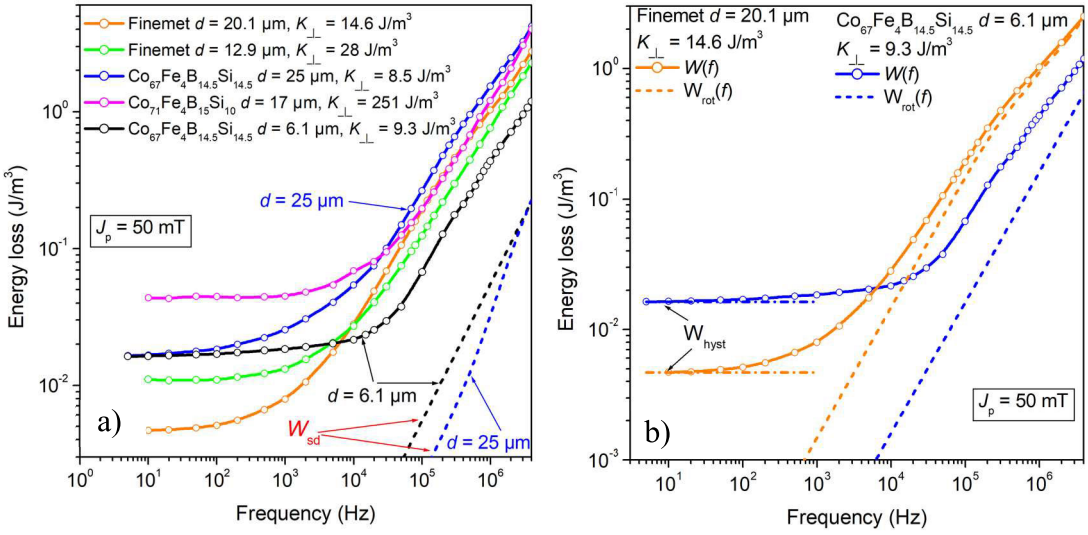

FIGURE 13. a) The quasi-static energy loss W_{hyst}, roughly behaving as $K_{\perp}^{1/2}/J_s$, with J_s the saturation polarization, tends to be higher, for given J_p, where J_s is lower (i.e., the amorphous alloys). However, the role of thickness becomes predominant beyond some 10 kHz, where the decrease of $W(f)$ with decreasing ribbon thickness d is rooted in the decreasing eddy current rotational loss $W_{rot}(f)$. The loss contribution by spin damping $W_{sd}(f)$ is always negligible below 1 MHz. It is apparent in (b) how $W(f)$ in the softest 20.1μm thick Finemet alloy rapidly overcomes beyond some 10 kHz the loss exhibited by the very thin ($d = 6.1\mu$m) Cobased amorphous alloy by the action of $W_{rot}(f)$.

is equally found in Fig. 9b and can be recognized in the transition region 1 kHz -100 kHz of $W(f)$, measured on two Finemet samples between 2 mT and 500 mT, in Fig. 10. Further analysis and comparison made in Fig. 11 show that in the extra-thin ($d = 6.1$ μm) $Co_{67}Fe_4B_{14.5}Si_{14.5}$ ribbon the eddy currents are decreased to the point that the spin-damping component $W_{sd}(f) = W_{rot}(f) - W_{eddy}(f)$ emerges already at low frequencies. $W_{sd}(f)$ plays the role of ultimate insuppressible loss contribution.

Of the many parameters affecting the magnetic loss in these materials, thickness plays an obvious prominent role, but the associated phenomenology, not exclusively related to eddy currents, does not lend itself to simple interpretation. We observe in Fig. 12a that the increase of W_{hyst}ensuing from the thinning of the Finemet ribbons is compensated by a decrease of the dynamic loss, to an extent and at a frequency depending on the J_p value. The higher J_p (here ranging between 2 mT and 500 mT), the higher the frequency at which this event occurs. In fact, quasi-static and dynamic losses exhibit $J_p^{2.44}$ and J_p^2 dependences, respectively (Fig. 12b). Final coalescing of the different $W(f)$ curves beyond some 10 MHz highlights the specific role of the actual constitutive equation and its parameters. We can nevertheless conclude, looking at the comprehensive comparison among representative amorphous and Finemet ribbons shown in Fig. 13a, that the latter exhibit a definite loss advantage up to the kHz range, whatever the thickness. This is qualitatively understood in terms of the dependence of W_{hyst} on the quantity $(K_{\perp\_})^{1/2}/J_s$. The benefit of decreased thickness on the dynamic losses is instead apparent, independent of the specific alloy, in the application-oriented kHz - MHz range. The loss ratio of around seven between the 25 μm and 6.1 μm thick $Co_{67}Fe_4B_{14.5}Si_{14.5}$ ribbons found in this range, intermediate between linear and squared dependence on d, points to an exchange-field mitigated skin effect [25]. We realize in the same figure how the spin-damping term $W_{sd}(f)$ can only marginally contribute to $W(f)$.

VI. CONCLUSION

We have performed a comprehensive experimental investigation on the broadband (DC – 1 GHz) permeability and loss properties of amorphous and nanocrystalline ribbons of thickness ranging between 6.1 μm and 25 μm, tested as tapewound ring samples. The experiments and their theoretical assessment have been focused on the transverse anisotropy materials, whose quasi-linear response, very-low loss figure at high and low frequencies, excellent broadband response, and general versatility are of utmost interest in power electronics. The magnetic properties brought to light in this work and their theoretical assessment can be summarized as follows: 1) Loss minimization is observed, for all compositions, by changing the induced anisotropy from longitudinal ($K_{//}$) to transverse ($K_{\perp\_}$). 2) The analysis of the dw dynamics in the $K_{\perp\_}$ ribbons by stroboscopic Kerr imaging shows, for defined polarization swing, progressive hindering of the dw displacements with frequency, 3) A picture emerges of dw-generated loss at low frequencies superseded by rotations at high frequencies. This conforms to modeling by loss decomposition, where the rotational contribution $W_{rot}(f)$ is lumped in the concept of classical loss. 4) By moving deep into the MHz range, the rotational loss behaves at odds with the conventional derivation of the classical eddy current loss by Maxwell's diffusion equation, where the permeability μ_{DC} is taken as the magnetic constitutive

equation. Consequently, a frequency-dependent constitutive equation is derived, by which the spin precession around the anisotropy field is derived using the Landau-Lifshiz equation. 5) The rotational loss is eventually calculated, by assuming appropriate values of α (damping constant), N_{dz} (demagnetizing coefficient), and l_e (exchange length). The loss separation between dw-generated and rotation-generated components leads to a consistent assessment of the experimental loss across a matrix of materials, polarization values, and frequencies. 6) The different broadband responses of amorphous and Finemet alloys and the role of ribbon thickness are brought to light and discussed.

We have shown, in conclusion, how physical concepts and modeling, embodied by the loss decomposition and its implementation over a comprehensive frequency band, can lead, via the combined solution of the Landau-Lifshitz and Maxwell's equations, to a general quantitative assessment of the magnetic properties of nanocrystalline and amorphous alloys having superior energetic efficiency.

APPENDIX

We derive the coupled solution of (13) and (14) under suitable boundary conditions. Given the even symmetry of the problem, the coordinate z can be restricted to $0 \le z \le d/2$, and the following boundary conditions apply

$$\left.\frac{\partial h_y}{\partial z}\right|_{z=0} = 0, \tag{A1}$$

and

$$\left.\frac{\partial^3 h_y}{\partial z^3}\right|_{z=0} = 0. \tag{A2}$$

By integrating (13) over the sample thickness and imposing the peak value B_p of the thickness-averaged induction, the further boundary condition is obtained

$$\left.\frac{\partial h_y}{\partial z}\right|_{z=d/2} = j\omega\sigma B_p d/2. \tag{A3}$$

Since the following Neumann boundary condition holds on m_y,

$$\left.\frac{\partial m_y}{\partial z}\right|_{z=d/2} = 0, \tag{A4}$$

and from (13), (A3), and (A4) we obtain

$$\begin{aligned}\left.\frac{\partial^3 h_y}{\partial z^3}\right|_{z=d/2} &= j\omega\sigma\mu_0\left(\left.\frac{\partial h_y}{\partial z}\right|_{z=d/2} + \left.\frac{\partial m_y}{\partial z}\right|_{z=d/2}\right)\\ &= -\omega^2\sigma^2\mu_0 B_p d/2.\end{aligned} \tag{A5}$$

We eliminate m_y by replacing (13) in (14), to obtain

$$\begin{aligned}&\chi(\omega) l_e^2 \frac{\partial^4 h_y}{\partial z^4} - \left(1 + j\omega\sigma\mu_0\chi(\omega) l_e^2\right)\frac{\partial^2 h_y}{\partial z^2}\\ &+ j\omega\sigma\mu_0(1+\chi(\omega)) h_y = 0,\end{aligned} \tag{A6}$$

Equation (A6) can be solved analytically together with the boundary conditions (A1), (A2), (A3), (A5), providing the magnetic field and the magnetization profile along the thickness. The solution of (27) is then

$$h_y(z) = C_1\frac{\cosh(\lambda_1 z)}{\sinh(\lambda_1 d/2)} + C_2\frac{\cosh(\lambda_2 z)}{\sinh(\lambda_2 d/2)} \tag{A7}$$

where λ_1 and λ_2 are the solution of the biquadratic algebraic equation

$$\begin{aligned}&\chi(\omega) l_e^2\lambda^4 - \left(1 + j\omega\sigma\mu_0\chi(\omega) l_e^2\right)\lambda^2\\ &+ j\omega\sigma\mu_0(1+\chi(\omega)) = 0,\end{aligned} \tag{A8}$$

Equation (A7) naturally satisfies the boundary conditions (A1) and (A2), but Eqs. (A3) and (A5) are satisfied only through suitable values of C_1 and C_2, which are obtained by solving the algebraic system

$$\begin{pmatrix}\lambda_1\coth\left(\lambda_1\frac{d}{2}\right) & \lambda_2\coth\left(\lambda_2\frac{d}{2}\right)\\ \lambda_1^3\coth\left(\lambda_1\frac{d}{2}\right) & \lambda_2^3\coth\left(\lambda_2\frac{d}{2}\right)\end{pmatrix} \cdot \begin{pmatrix}C_1\\ C_2\end{pmatrix} = \begin{pmatrix}\omega\sigma B_p\frac{d}{2}\\ -\omega^2\sigma^2\mu_0 B_p\frac{d}{2}\end{pmatrix} \tag{A9}$$

REFERENCES

[1] F. Neveu, B. Allard, C. Martin, P. Bevilacqua, and F. Voiron, "A 100 MHz 91.5% peak efficiency integrated buck converter with a three-MOSFET cascode bridge," *IEEE Trans. Power Electron.*, vol. 31, no. 6, pp. 3985–3988, Jun. 2016, doi: 10.1109/TPEL.2015.2502058.

[2] A. J. Hanson, J. A. Belk, S. Lim, C. R. Sullivan, and D. J. Perreault, "Measurements and performance factor comparisons of magnetic materials at high frequency," *IEEE Trans. Power Electron.*, vol. 31, no. 11, pp. 7909–7925, Nov. 2016, doi: 10.1109/TPEL.2015.2514084.

[3] M. Mu, Q. Li, D. J. Gilham, F. C. Lee, and K. D. T. Ngo, "New core loss measurement method for high-frequency magnetic materials," *IEEE Trans. Power Electron.*, vol. 29, no. 8, pp. 4374–4381, Aug. 2014, doi: 10.1109/TPEL.2013.2286830.

[4] W. Martinez and C. Suarez, "Current measurement issues of a high frequency GaN inverter in the MHz order for magnetic characterization," in *Proc. IEEE Appl. Power Electron. Conf. Expo. (APEC)*, Mar. 2019, pp. 2728–2733, doi: 10.1109/APEC.2019.8721844.

[5] W. Shen, F. Wang, D. Boroyevich, and C. W. Tipton, "Loss characterization and calculation of nanocrystalline cores for high-frequency magnetics applications," *IEEE Trans. Power Electron.*, vol. 23, no. 1, pp. 475–484, Jan. 2008, doi: 10.1109/TPEL.2007.911881.

[6] J. Füzerová, J. Füzer, P. Kollár, R. Bureš, and M. Fáberová, "Complex permeability and core loss of soft magnetic Fe-based nanocrystalline powder cores," *J. Magn. Magn. Mater.*, vol. 345, pp. 77–81, Nov. 2013, doi: 10.1016/j.jmmm.2013.06.008.

[7] D. Rodriguez-Sotelo, M. A. Rodriguez-Licea, I. Araujo-Vargas, J. Prado-Olivarez, A.-I. Barranco-Gutiérrez, and F. J. Perez-Pinal, "Power losses models for magnetic cores: A review," *Micromachines*, vol. 13, no. 3, p. 418, Mar. 2022, doi: 10.3390/mi13030418.

[8] T. Dimier and J. Biela, "Eddy current loss model for ferrite ring cores based on a meta-material model of the core properties," *IEEE Trans. Magn.*, vol. 58, pp. 1–5, 2022, doi: 10.1109/TMAG.2021.3084812.

[9] S. Dobák, C. Beatrice, V. Tsakaloudi, and F. Fiorillo, "Magnetic losses in soft ferrites," *Magnetochemistry*, vol. 8, no. 6, p. 60, Jun. 2022, doi: 10.3390/magnetochemistry8060060.

[10] H. Schwenk, J. Beichler, W. Loges, and C. Scharwitz, "Actual and future developments of nanocrystalline magnetic materials for common mode chokes and transformers," in *Proc. PCIM Eur. Int. Exhib. Conf. Power Electron., Intell. Motion, Renew. Energy Energy Manage.*, Nuremberg, Germany, May 2015, pp. 1–8.

[11] F. C. Li, T. Liu, J. Y. Zhang, S. Shuang, Q. Wang, A. D. Wang, J. G. Wang, and Y. Yang, "Amorphous–nanocrystalline alloys: Fabrication, properties, and applications," *Mater. Today Adv.*, vol. 4, Dec. 2019, Art. no. 100027, doi: 10.1016/j.mtadv.2019.100027.

[12] C. Jiang, X. Li, S. S. Ghosh, H. Zhao, Y. Shen, and T. Long, "Nanocrystalline powder cores for high-power high-frequency power electronics applications," *IEEE Trans. Power Electron.*, vol. 35, no. 10, pp. 10821–10830, Oct. 2020, doi: 10.1109/TPEL.2020.2979069.
[13] S. Flohrer, R. Schäfer, C. Polak, and G. Herzer, "Interplay of uniform and random anisotropy in nanocrystalline soft magnetic alloys," *Acta Mater.*, vol. 53, no. 10, pp. 2937–2942, Jun. 2005, doi: 10.1016/j.actamat.2005.03.008.
[14] M. Deng, Y. Yang, P. Fu, S. Liang, X. Fu, W. Cai, and P. Tao, "Core-loss behavior of Fe-based nanocrystalline at high frequency and high temperature," *J. Mater. Sci., Mater. Electron.*, vol. 35, no. 12, Apr. 2024, Art. no. 856, doi: 10.1007/s10854-024-12600-w.
[15] Y. Cao, F. Yang, J. Li, A. He, A. Wang, H. Xiao, Y. Dong, X. Liu, B. Zhang, and Y. Han, "High-frequency magnetic characteristics and operating thermal stability of industrialized $Fe_{76}Si_{13}B_8Nb_2Cu_1$ nanocrystalline alloy," *J. Magn. Magn. Mater.*, vol. 526, May 2021, Art. no. 167691, doi: 10.1016/j.jmmm.2020.167691.
[16] S. Flohrer, R. Schafer, J. Mccord, S. Roth, L. Schultz, and G. Herzer, "Magnetization loss and domain refinement in nanocrystalline tape wound cores," *Acta Mater.*, vol. 54, no. 12, pp. 3253–3259, Jul. 2006, doi: 10.1016/j.actamat.2006.03.011.
[17] S. Flohrer, R. Schafer, J. Mccord, S. Roth, L. Schultz, F. Fiorillo, W. Gunther, and G. Herzer, "Dynamic magnetization process of nanocrystalline tape wound cores with transverse field-induced anisotropy," *Acta Mater.*, vol. 54, no. 18, pp. 4693–4698, Oct. 2006, doi: 10.1016/j.actamat.2006.04.040.
[18] G. Herzer, "Modern soft magnets: Amorphous and nanocrystalline materials," *Acta Mater.*, vol. 61, no. 3, pp. 718–734, Feb. 2013, doi: 10.1016/j.actamat.2012.10.040.
[19] H. Fukunaga, T. Yanai, H. Tanaka, M. Nakano, K. Takahashi, Y. Yoshizawa, K. Ishiyama, and K. I. Arai, "Nanostructured metallic cores with extremely low loss and controlled permeability," *IEEE Trans. Magn.*, vol. 38, no. 5, pp. 3138–3140, Sep. 2002, doi: 10.1109/TMAG.2002.802421.
[20] J. Petzold, "Applications of nanocrystalline softmagnetic materials for modern electronic devices," *Scripta Mater.*, vol. 48, no. 7, pp. 895–901, Apr. 2003, doi: 10.1016/s1359-6462(02)00624-3.
[21] A. Ravera, A. Oliveri, M. Lodi, C. Beatrice, E. Ferrara, F. Fiorillo, and M. Storace, "Modeling amorphous core inductors up to magnetic saturation," *IEEE Trans. Power Electron.*, early access, Sep. 18, 2024, doi: 10.1109/TPEL.2024.3463803.
[22] L.-G. Petrescu, M.-C. Petrescu, E. Cazacu, and C.-D. Constantinescu, "Estimation of energy losses in nanocrystalline FINEMET alloys working at high frequency," *Materials*, vol. 14, no. 24, p. 7745, Dec. 2021, doi: 10.3390/ma14247745.
[23] C. Feng, Y. Zhang, and Q. Chi, "Design of a novel rotary transformer with accurate prediction of nanocrystalline alloy core loss using improved steinmetz formulation," *IEEE Trans. Ind. Appl.*, vol. 60, no. 2, pp. 2764–2772, Mar. 2024, doi: 10.1109/TIA.2023.3348776.
[24] H. Chazal, A. Kedous-Lebouc, and T. Waeckerle, "Characterization and modeling of high-frequency behavior of nanocrystalline alloys," *J. Magn. Magn. Mater.*, vol. 304, no. 2, pp. e798–e800, Sep. 2006, doi: 10.1016/j.jmmm.2006.02.227.
[25] G. Bertotti, *Hysteresis in Magnetism*. San Diego, CA, USA: Academic, 1998.
[26] M. A. Willard, T. Francavilla, and V. G. Harris, "Core-loss analysis of an (Fe, Co, Ni)-based nanocrystalline soft magnetic alloy," *J. Appl. Phys.*, vol. 97, no. 10, May 2005, Art. no. 10F502, doi: 10.1063/1.1847333.
[27] C. Serpico, I. D. Mayergoyz, and G. Bertotti, "Analysis of eddy currents with Landau–Lifshitz equation as a constitutive relation," *IEEE Trans. Magn.*, vol. 37, no. 5, pp. 3546–3549, Sep. 2001, doi: 10.1109/20.952658.
[28] L. Dupré, F. Olyslager, and J. Melkebeek, "Macroscopic fields in thin ferromagnetic sheets taking into account eddy currents and Landau–Lifshitz magnetization," *J. Magn. Magn. Mater.*, vols. 272–276, pp. 717–719, May 2004, doi: 10.1016/j.jmmm.2003.11.259.
[29] K. Seemann, H. Leiste, and V. Bekker, "New theoretical approach to the RF-dynamics of soft magnetic FeTaN films for CMOS components," *J. Magn. Magn. Mater.*, vol. 278, nos. 1–2, pp. 200–207, Jul. 2004, doi: 10.1016/j.jmmm.2003.11.402.
[30] O. Bottauscio, F. Fiorillo, C. Beatrice, A. Caprile, and A. Magni, "Modeling high-frequency magnetic losses in transverse anisotropy amorphous ribbons," *IEEE Trans. Magn.*, vol. 51, no. 3, pp. 1–4, Mar. 2015, doi: 10.1109/TMAG.2014.2361534.
[31] F. Fiorillo, "Measurements of magnetic materials," *Metrologia*, vol. 47, pp. S114–S142, Jun. 2010, doi: 10.1088/0026-1394/47/2/S11.
[32] A. Magni, F. Fiorillo, A. Caprile, E. Ferrara, and L. Martino, "Fluxmetric-magnetooptical approach to broadband energy losses in amorphous ribbons," *J. Appl. Phys.*, vol. 109, no. 7, Apr. 2011, Art. no. 07A322, doi: 10.1063/1.3556937.
[33] A. Magni, C. Beatrice, O. Bottauscio, A. Caprile, E. Ferrara, and F. Fiorillo, "Magnetization process in thin laminations up to 1 GHz," *IEEE Trans. Magn.*, vol. 48, no. 4, pp. 1363–1366, Apr. 2012, doi: 10.1109/TMAG.2011.2172934.
[34] G. Bertotti, "General properties of power losses in soft ferromagnetic materials," *IEEE Trans. Magn.*, vol. 24, no. 1, pp. 621–630, Jan. 1988, doi: 10.1109/20.43994.

CARLO STEFANO RAGUSA (Senior Member, IEEE) was born in Catania, Italy. He received the M.Sc. degree in electrical engineering from the University of Catania, in 1993, and the Ph.D. degree in electrical engineering from the Politecnico di Torino, Turin, Italy, in 1997. He has been a Faculty Member of the Politecnico di Torino, since 1998, where he is currently a Full Professor of electrical engineering with the Department of Energy "Galileo Ferraris." His research interests include the experimental characterization and modeling of soft magnetic materials for electrotechnical applications and the analysis and optimization of electromagnetic devices. He has been a member of the International Organizing Committee of the Soft Magnetic Materials Conference, since 2015, and the Chairperson of the Steering Committee of the International Workshop on 1-D and 2-D Magnetic Measurement and Testing, since 2016. He has been the Chair of the IEC/TC 68 Magnetic Alloys and Steels, since 2020.

SAMUEL DOBÁK (Member, IEEE) received the master's and Ph.D. degrees in condensed matter physics from P. J. Šafárik University (UPJŠ), Košice, Slovakia, in 2014 and 2018, respectively. From 2015 to 2019, he conducted several research stays with the Istituto Nazionale di Ricerca Metrologica, Turin, Italy, where he investigated broadband magnetic losses in alloys and spinel ferrites. He is currently a Senior Research Scientist with the Institute of Physics, Faculty of Science, UPJŠ. His research interest includes magnetisation process.

CINZIA BEATRICE was born in Turin, Italy, in 1958. She received the degree in physics from the University of Modena, in 1982, and the Ph.D. degree in physics from the Politecnico di Torino, Turin, in 1987. She has been a Research Scientist with the Materials Department, Istituto Elettrotecnico Nazionale Galileo Ferraris (currently Istituto Nazionale di Ricerca Metrologica—INRIM), Turin, since 1987, where she has held the position of a Senior Researcher, since 1997. Her research has covered many aspects of the magnetisation process in soft and permanent magnetic materials, such as hysteresis, energy losses, Barkhausen noise, and thermal relaxation effects.

LUIGI SOLIMENE (Member, IEEE) was born in Avellino, Italy, in 1994. He received the B.S., M.S., and Ph.D. degrees in electrical engineering from the Politecnico di Torino, Turin, Italy, in 2016, 2019, and 2022, respectively. From 2022 to 2023, he was a Research Fellow with the Department of Energy "Galileo Ferraris," Politecnico di Torino, where he is currently an Assistant Professor. His research interests include the theoretical analysis, experimental characterization, and optimization of magnetic materials and devices for electrical energy conversion.

ALESSANDRO MAGNI received the Ph.D. degree in physics from the Politecnico of Turin, Italy, in 1998, working in the group of Prof. G. Bertotti, with the dissertation "Magnetization Dynamics and Hysteresis in the Framework of the Domain Theory." From 1999 to 2003, he was a Postdoctoral Fellow with the Materials Unit, Istituto Elettrotecnico Nazionale (IEN) Galileo Ferraris. Since 2004, he has been a Researcher with the Materials and Life Sciences Department, Istituto Nazionale di Ricerca Metrologica—INRIM, Turin; and the Head of the Magnetoptical Laboratory. He is the co-author of more than 100 articles in peer-reviewed journals. His research is focused on the collective properties of complex systems, studied from the point of view of their magnetic properties, particularly domain structure and the effect of electrical and spin currents, investigated by magneto-optical methods.

FAUSTO FIORILLO received the Laurea degree from the University of Torino, in 1972. He started his career as a Physicist with the Istituto Elettrotecnico Nazionale Galileo Ferraris (currently Istituto Nazionale di Ricerca Metrologica—INRIM), in 1974. He has been the Research Director with INRIM till his retirement, in 2012. He is currently an Emeritus Scientist with INRIM. He has authored/co-authored 240 peer-reviewed publications in international scientific journals, review monographs, and chapters on international series on magnetic materials. He is the author of the comprehensive treatise *Measurement and Characterization of Magnetic Materials* (Academic Press-Elsevier, December 2004). His scientific work and research interests include the properties of magnetic materials and their measurement.

Open Access funding provided by 'Politecnico di Torino' within the CRUI CARE Agreement